SANDIA REPORT SAND2021-11344 Printed September 2021



Transient Deformation in Additively Manufactured 316L Stainless Steel Lattices Characterized with in-situ X-ray Phase Contrast Imaging: The Complete Dataset for Three Geometrical Lattices

Brittany A. Branch, Paul E. Specht, Scott Jensen, and Bradley Jared

Prepared by Sandia National Laboratories Albuquerque, New Mexico 87185 and Livermore, California 94550 Issued by Sandia National Laboratories, operated for the United States Department of Energy by National Technology & Engineering Solutions of Sandia, LLC.

NOTICE: This report was prepared as an account of work sponsored by an agency of the United States Government. Neither the United States Government, nor any agency thereof, nor any of their employees, nor any of their contractors, subcontractors, or their employees, make any warranty, express or implied, or assume any legal liability or responsibility for the accuracy, completeness, or usefulness of any information, apparatus, product, or process disclosed, or represent that its use would not infringe privately owned rights. Reference herein to any specific commercial product, process, or service by trade name, trademark, manufacturer, or otherwise, does not necessarily constitute or imply its endorsement, recommendation, or favoring by the United States Government, any agency thereof, or any of their contractors. The views and opinions expressed herein do not necessarily state or reflect those of the United States Government, any agency thereof, or any of their contractors.

Printed in the United States of America. This report has been reproduced directly from the best available copy.

Available to DOE and DOE contractors from

U.S. Department of Energy Office of Scientific and Technical Information P.O. Box 62 Oak Ridge, TN 37831

Telephone: (865) 576-8401 Facsimile: (865) 576-5728 E-Mail: reports@osti.gov

Online ordering: http://www.osti.gov/scitech

Available to the public from

U.S. Department of Commerce National Technical Information Service 5301 Shawnee Rd Alexandria, VA 22312

Telephone: (800) 553-6847 Facsimile: (703) 605-6900 E-Mail: orders@ntis.gov

Online order: https://classic.ntis.gov/help/order-methods/



ABSTRACT

Metallic lattice structures are being considered for shock mitigation applications due to their superior mechanical properties, energy absorption capability and lightweight characteristics inherent of the additive manufacturing process. In this study, shock compression experiments coupled to x-ray phase contrast imaging (PCI) were conducted on 316L stainless steel lattices. Meso-scale simulations incorporating the as-built lattice structure characterized by computed tomography were used to simulate PCI radiographs in CTH for direct comparison to experimental data. The methodology presented here offers robust validation for constitutive properties to further our understanding of lattice compaction at application-relevant strain rates.

ACKNOWLEDGEMENTS

The authors would like to acknowledge the contribution of materials manufacturing by David Saiz and computed tomography characterization by David Moore and Eddie Moffitt conducted at Sandia National Laboratories. The octet geometry studied here was leveraged from the AM Lattice Access Collaborative Team project led by Jonathan Pegues. The authors would also like to thank the staff at the Dynamic Compression Sector where shock compression experiments were performed, which is operated by Washington State University under the U.S. Department of Energy (DOE)/National Nuclear Security Administration award no. DE-NA0002442. Brittany Branch would like to specially thank Paul Specht for the many hallway conversations leading to this work! Sandia National Laboratories is a multi-mission laboratory managed and operated by National Technology & Engineering Solutions of Sandia, LLC, a wholly owned subsidiary of Honeywell International Inc., for the U.S. Department of Energy's National Nuclear Security Administration under contract DE-NA0003525. This paper describes objective technical results and analysis. Any subjective views or opinions that might be expressed in the paper do not necessarily represent the views of the U.S. Department of Energy or the United States Government.

CONTENTS

1.	Introduction		
2.	methods	11	
	2.1. Laser Powder Bed Additive Manufacturing	11	
	2.2. Meso-Scale Modeling	12	
	2.2.1. CTH Rendering of the As-built Lattice	12	
	2.2.2. Modeling the Compaction Response in CTH	13	
	2.3. Shockwave Experiments	13	
3.	Results & Discussion	16	
4.	Conclusions	20	
LI	T OF FIGURES		
Fig	are 1. Micro X-ray computed tomography three-dimensional renderings of the 316L stainless steel lattice geometries at different visual angles and the designated sample number (shown at the bottom) for the single-x (SN57), double-x (SN-89) and octet configurations (SN1-3)	11	
Fig	are 2. Two-dimensional CT slice of the as-built SN01 lattice (a) and a binary representation used for generating the 3D geometry in CTH.	12	
	are 3. Schematic illustrating the shock compression experiment coupled to phase contrast imaging with the stainless-steel metal lattice affixed to a target holder at the end of the gun barrel and x-rays transmitting out of the page through the impact edge of the lattice to the PCI detector system. The corresponding static PCI image and CTH rendering with the as-built SN01 lattice is also shown. The black box shows the approximate area used to generate a synthetic radiograph to compare to the PCI images	o e	
Fig	are 4. PCI image of the compaction on lattice SN01 (Top) and the simulated radiographs generated by CTH (bottom). The numbers above each image set represent the timing of the images in nanoseconds relative to the triggering event.	16	
Fig	are 5. PCI image of the compaction of lattice SN02 (Top) and the simulated radiographs generated by CTH (bottom). The numbers above each image set represent the timing of the images in nanoseconds relative to the triggering event.		
Fig	are 6. PCI image of the compaction of lattice SN03 (Top) and the simulated radiographs generated by CTH (bottom). The numbers above each image set represent the timing of the images in nanoseconds relative to the triggering event		
Fig	are 7. PCI image of the compaction of lattice SN57 (Top) and the simulated radiographs generated by CTH (bottom). The numbers above each image set represent the timing of the images in nanoseconds relative to the triggering event	18	
Fig	are 8. PCI image of the compaction of lattice SN89 (Top) and the simulated radiographs generated by CTH (bottom). The numbers above each image set represent the timing of the images in nanoseconds relative to the triggering event		
Fig	are 9. PCI image of the compaction of lattice SN01 (PCI) and the simulated radiographs generated by CTH for various strength models: using the calibrated SG parameters and the initial yield point as determined through quasi-static measurements (Cal.), an elastically-perfectly-plastic model using an initial yield point as defined by quasi-static measurements (EPP), a SG model with the initial yield point set at the maximum for strain		

hardening (High Y), and a purely hydrodynamic simulations with no strength model (Hydro). The choice of strength model is seen to alter the shape of the compaction wave, with the hydrodynamic case generating a significant amount of ejecta19
LIST OF TABLES
Table 1. Summary of measured projectile velocity and the lattice geometry along with sample designation for each experiment conducted

ACRONYMS AND DEFINITIONS

Abbreviation	Definition
PCI	Phase Contrast Imaging
CAD	Computer Aided Design
СТ	Computed tomography
SMASH	Sandia Matlab Analysis Hierarchy
DCS	Dynamic Compression Sector
APS	Advanced Photon Source
FOV	Field of View
EOS	Equation of State
SG	Steinberg-Guinan
AMR	Adaptive mesh refinement

1. INTRODUCTION

Lattice structures are becoming increasingly important in the automotive, aerospace and defense industries that require lightweight structural components for load bearing and energy absorption applications.¹ These periodic cellular structures can be tailored to have superior vibrational behavior,² mechanical properies³⁻¹⁰ and energy absorption performance¹¹⁻¹⁵ due to their high stiffness and strength at a low relative density.^{16,17} Through the years, there have been numerous efforts to characterize the effects of the manufacturing processing parameters and the resulting topology on the mechanical properties of metal lattices.¹⁸⁻²⁴ More recently, in-situ materials characterization utilizing synchrotron radiation light sources for x-ray diffraction and imaging measurements has revolutionized efforts in model validation and improved our understanding of the process ²⁵⁻³⁰ and topology^{31,32} effects of metal lattices. But to date, in situ x-ray measurements have not been employed to understand the compaction response ^{33,34} at application-relevant strain rates despite these materials being primary candidates for shockwave mitigation barriers due to their interface dominated structure.³⁵

Current advancements of pairing shock compression experiments with in-situ phase contrast imaging (PCI) enables the characterization of the predominate deformation mechanisms driving compaction in AM materials. Thus far these studies have been limited to polymers. These efforts used meso-scale simulations utilizing the idealized three-dimensional structure generated from a computer aided design (CAD) file to make qualitative comparisons to the PCI radiographs and infer material properties from the observed deviatoric (shear) and volumetric (pressure) response. These idealized simulations ignore manufacturing discrepancies such as enlarged strut diameters, porosity and other common printing defects which can affect the observed mechanical response. This lack of comparison with PCI radiographs weakens the relationships inferred from these efforts.

Here, we demonstrate shockwave dynamics in 316L stainless steel lattices using x-ray phase contrast imaging and report a methodology to perform detailed simulations that incorporate the as-built lattice characterized by computed tomography into the finite-volume hydrocode CTH v12.0 ³⁹ to produce simulated radiographs for direct comparison. Our work illustrates, for the first time, a robust validation method for the constitutive modeling of transient deformation states during the compaction in metal lattices while accounting for common build defects, such as porosity and broken/misshapen struts, or printing irregularities such as strut diameter. These results open the possibility of understanding material behavior beyond topological effects towards material properties that are highly dependent on the manufacturing process and have previously been disregarded.

2. METHODS

2.1. Laser Powder Bed Additive Manufacturing

Additively manufactured lattices in three geometries were fabricated using a laser powder bed fusion (LPBF) system, ProX DMP 200 (3D systems): octet, single-x, and double-x. Figure 2 shows three-dimensional renderings at three different views of the three lattice geometries tested. The ProX DMP 200 incorporates a continuous 1070 nm Yb-fiber laser which was focused roughly 1 mm above the powder layer with a 1/e² spot size approximately 50 μm at the beam waist. The incident laser power was 113 W with a scan speed of 1400 mm/s. Two laser scan patterns were used depending on the lattice geometry printed. For the octet geometry a "normal" configuration was used, which raster each part sequentially with scan lines alternating between layers being parallel/anti-parallel to the powder feed direction (0°) or perpendicular (90°). The single and double X designs used a hexagonal hatch pattern where each layer scan direction alternated between 45° and 135°. Laser scan paths and machine instructions were generated using the 3D systems proprietary software, 3DXpert. The three different geometries were produced on a single build plate. The feedstock powder distribution was characterized using a Malvern 3000 (Malvern Panalytical) particle size analyzer and the 10th, 50th and 90th percentile for particle size were found to be 11.4, 23.1 and 42.6 µm, respectively. Powder composition was quantified on a Aspex using energy-dispersive x-ray spectroscopy (EDS) to be 59.6% Fe, 18.73% Cr, 8.36% Ni, 1.19% Mn, 1.69% O₂, 0.01% Si and 0.009% Al. Each layer of powder was spread by a roller to a 30 µm thickness and a constant flow of argon gas was used in the build chamber to maintain oxygen levels below 1000 ppm. After fabrication, parts were removed from the AISI 430F stainless steel build plate using a Makino U6 wire EDM machine with 0.25mm diameter brass wire. The AM lattices were then characterized using x-ray computed tomography (CT) on a X3000 CT machine (220 kV and 7.5 watts) with Varex 2520DX x-ray detector system. Each lattice was scanned for 80 minutes at 2.75 frames per second with a filter of 0.25 mm of copper. Four frames were averaged to produce tiff stacks that fully captured the tortuous surface features, asymmetric cell structures and printing defects (Figure 1).

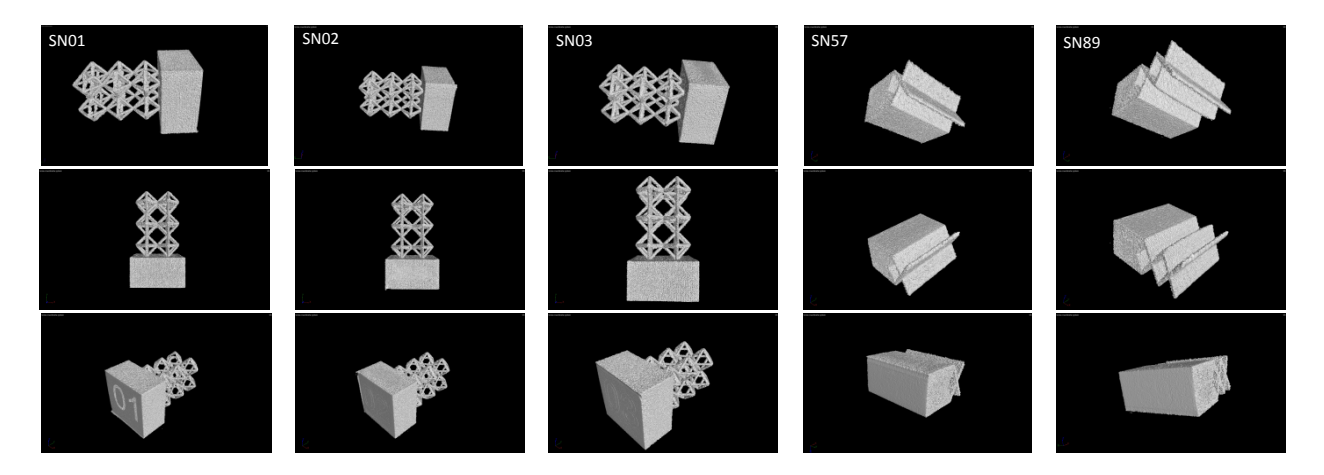


Figure 1. Micro X-ray computed tomography three-dimensional renderings of the 316L stainless steel lattice geometries at different visual angles and the designated sample

number (shown at the bottom) for the single-x (SN57), double-x (SN-89) and octet configurations (SN1-3).

2.2. Meso-Scale Modeling

2.2.1. CTH Rendering of the As-built Lattice

To incorporate the CT characterization of each lattice into CTH, 2D slices were generated from the CT scan and converted into binary images to clearly identify the AM 316L stainless steel as shown in Figure 2b. This was done with a simple MATLAB script using the Image class in the Sandia Matlab Analysis Hierarchy (SMASH) toolbox.⁴⁰ Each image was smoothed using a median filter and then a thresholding was applied to the intensity of each pixel. While some of the finer surface features are obscured due to the numerical smoothing, the method clearly captures the gross features of the lattice.

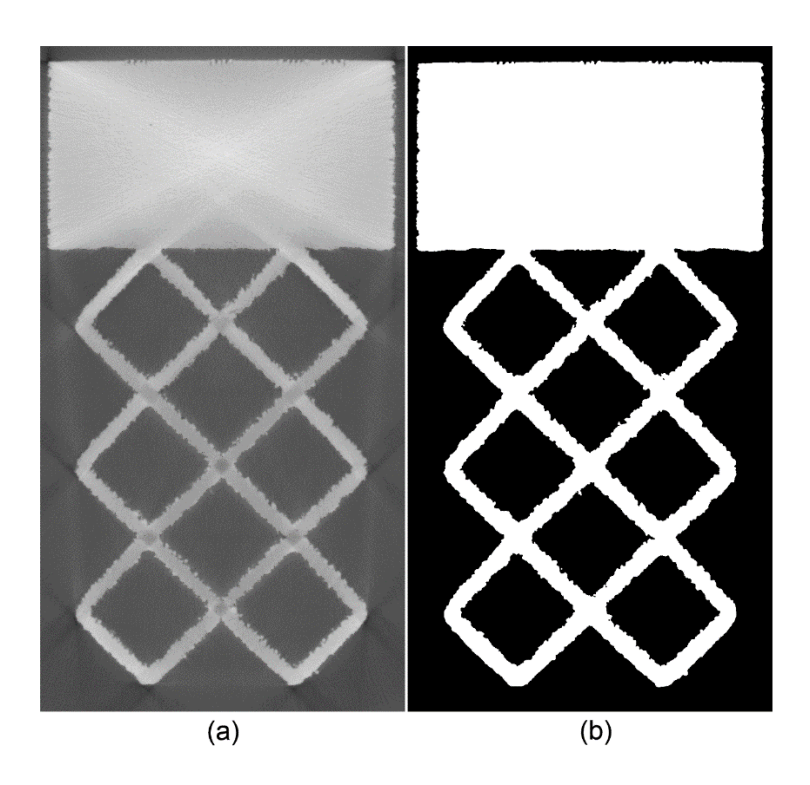


Figure 2. Two-dimensional CT slice of the as-built SN01 lattice (a) and a binary representation used for generating the 3D geometry in CTH.

Using this stack of 2D binary images of the lattice, a 3D representation of the lattice was rendered in CTH using a custom MATLAB script.⁴¹ This script traced the edges of the 316L SS lattice in each image, storing the coordinates of each point on the edge in pixels. These points are converted to x and y dimensions using the known voxel size of the CT scan. A user defined shape is generated in CTH using these x and y coordinates, defining the lattice boundary. The thickness of each user defined shape is set equal to the voxel size. These voxel thick slices were successively stacked until the entirety of the lattice was generated. While this method lacks elegance, generating input decks on the order of several hundred megabytes, it does render the

as-built geometry of the lattice to level of accuracy on the order of the CT scan. A CTH rendering of the as-built lattice using this methodology is shown below in Figure 3, where a clear printing error is seen in the lattice as indicated by the arrow. Such an anomaly would not have been captured using the CAD file used for printing the lattices to represent the geometry.

2.2.2. Modeling the Compaction Response in CTH

The simulation used the measured thickness of the impactor and the measured impact velocity. Semi-infinite boundary conditions were used along the X and Y boundaries along with the negative Z direction. The semi-infinite boundary condition allowed for simulation of only part of the Al backer and stainless-steel impactor. This was done to save computational resources, since wave reflection from the edges of the flier and projectile will not influence the results during the time of interest. The positive Z direction was given a voided boundary condition. Since the compaction wave never reached the positive Z boundary during the length of the simulations, this choice is inconsequential to the outcome of the simulations.

At these large impact velocities, significant off-Hugoniot behavior was expected. As a result, the equation of state (EOS) of the 316L SS was modeled using the SESAME 4270 table⁴⁵ and calibrated Steinberg-Guinan (SG) strength model parameters for 304L stainless steel.^{46,47} This is an approximation, especially given the issues with the SESAME 4270 formulation.⁴⁵ However, given that both 304L and 316L stainless steel are austenitic and have similar composition, this was deemed appropriate for the goals of this work. For the AM lattice, the initial yield point for the SG strength model was increased to 0.55 GPa to match quasi-static compression measurements.⁴⁸ The Al6061 projectile was modeled with the 3700 SESAME table⁴⁹ and parameterized SG model for Al6061.⁴⁷ Simple void insertion based on a tensile pressure threshold was used to approximate the failure response of all materials and interfaces. The impact plane was given an extremely low failure pressure to ensure that it would separate upon any tensile load.

For the simulations, the cell size in the lattice was kept to roughly the voxel size of the CT scans. While there is not a one-to-one alignment of the lattice and cells, given CTH is a Eulerian hydrocode, this was deemed to be a reasonable resolution to capture the geometric irregularities of the lattice. Adaptive mesh refinement (AMR) was used to reduce the computational cost of these simulations. Additionally, small flecks of material at non-physical conditions that slow the timestep were removed from the simulations. While this does not strictly conserve mass and momentum, the amount of material removed is extremely small and will have no effect on the results. Even with these measures, the simulations required up to 40 hours on 576 processors to run to completion.

2.3. Shockwave Experiments

Shockwaves were generated in the metal lattices by launching a wrought 316L stainless steel flier backed by an Al6061 projectile using the single-stage gas gun at the Dynamic Compression Sector (DCS) located at the Advanced Photon Source (APS) at Argonne National Laboratory. Table 1 shows the testing conditions for each lattice geometry. Since this gun is coupled to the synchrotron, time-resolved X-ray phase contrast imaging of the transient deformation of the lattice was possible. In situ imaging of shockwave behavior in AM polymer materials has been

described in detail previously. 42-44 Here we employ a similar technique, schematically shown in Figure 3, using pulsed x-rays 153.4 nanoseconds apart with a 80 picosecond width (24-bunch mode at APS) and a photon energy of 25 keV. The x-rays transmitted through the lattice are detected producing eight images of the transient deformation of the lattice per experiment with a field of view (FOV) of \sim 2.5 mm . Given the limited x-ray penetration depths of the high Z stainless steel, strut spacing of the lattice was optimized to allow sufficient voided space within the FOV to observe the compaction dynamics.

Table 1. Summary of measured projectile velocity and the lattice geometry along with sample designation for each experiment conducted.

Shot #	Lattice Sample Name	Lattice Geometry	Projectile Velocity (km/s)
20-2-053	SN01	Octet	0.604
20-1-040	SN02	Octet	1.259
20-2-054	SN03	Octet	0.756
20-2-059	SN57	Single X	0.805
20-2-061	SN89	Double X	0.801

These experimental conditions along with the as-built lattice were incorporated in the CTH simulations. To orient the lattice in the same manner as the experiment, a lattice number was printed on the bottom of the base plate. This enabled the impact and x-ray direction in the simulations to be easily matched to the experiment. Additionally, precise placement of the PCI field of view relative to the lattice boundary enabled easy generation of comparative simulated radiographs.

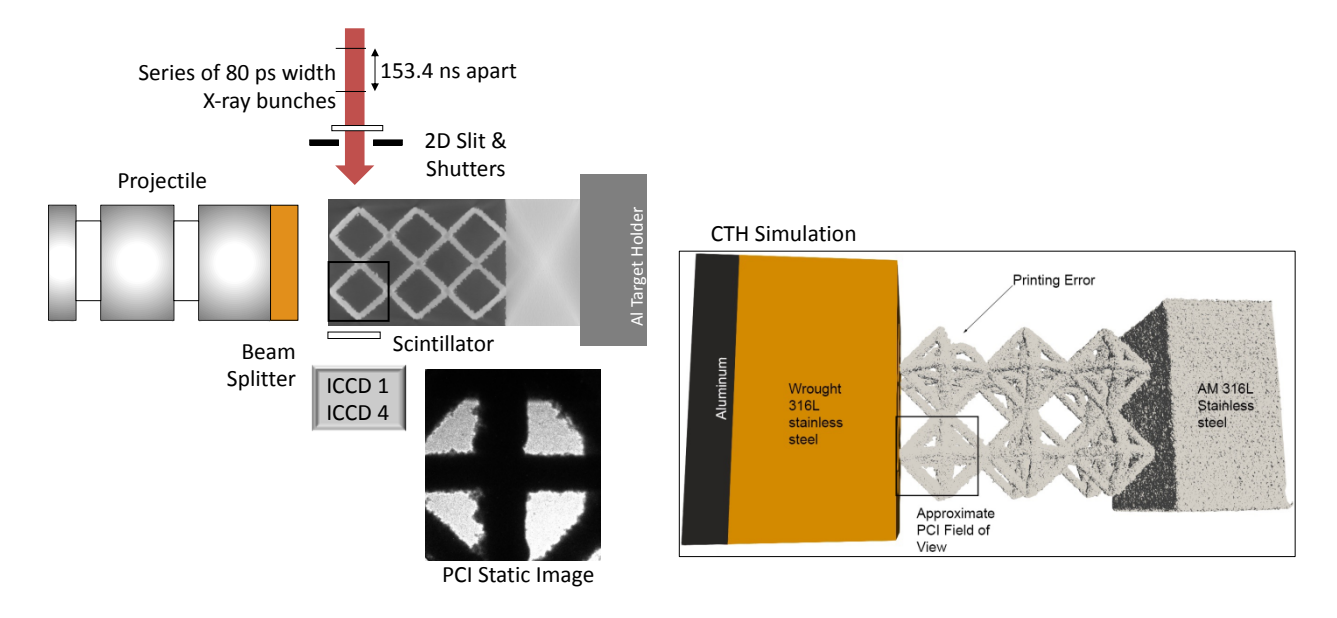


Figure 3. Schematic illustrating the shock compression experiment coupled to phase contrast imaging with the stainless-steel metal lattice affixed to a target holder at the end of the gun barrel and x-rays transmitting out of the page through the impact edge of the lattice to the PCI detector system. The corresponding static PCI image and CTH rendering with the as-built SN01 lattice is also shown. The black box shows the approximate area used to generate a synthetic radiograph to compare to the PCI images.

3. RESULTS & DISCUSSION

Using our methodology and the built-in function for generating synthetic radiographs available in CTH we can make direct comparisons between simulations and experiments during the compaction of a lattice.

Figure 4 shows the PCI image for the compaction of lattice SN01 (top) impacted at 0.604 km/s from left-to-right and the simulated radiographs generated by CTH (bottom) where the numbers above each set of images represent the timing of the images in nanoseconds relative to the triggering event. There is excellent agreement between the experimental PCI images and the simulated radiographs using this method. The first set of images (551.6 ns) in Figure 4 is before arrival of the flyer. In this set of images, the irregularities in the lattice seen in the PCI images are well captured by our methodology for incorporating the as-built geometry. As the compaction event proceeds in time, we see that the simulated radiographs capture the shape of the wave very well. While our simulations seem to slightly underpredict the speed of the compaction wave, it is on the order of uncertainties in the timing of the images. Considering the assumptions made in the EOS and strength model and uncertainties in timing of the images, this agreement is excellent.

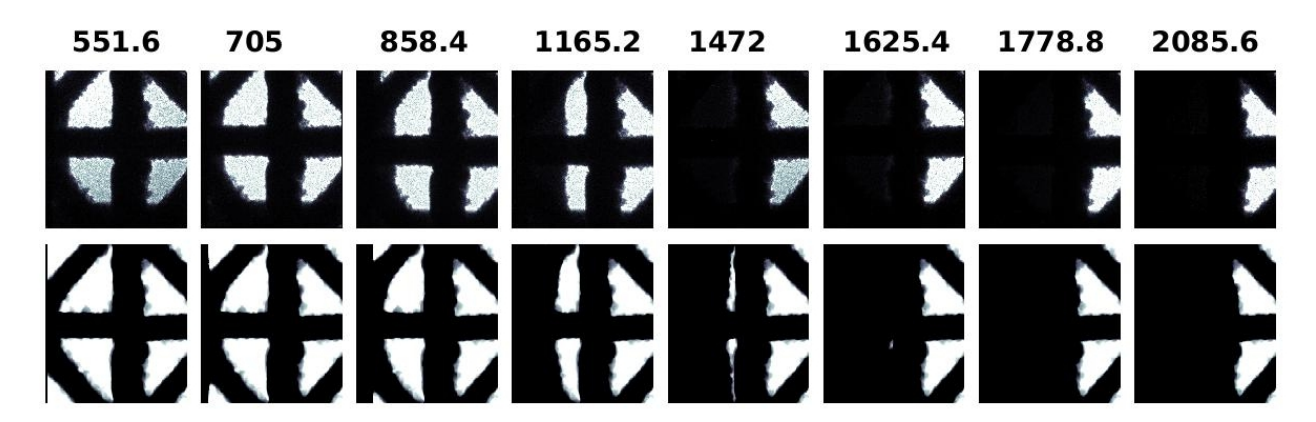


Figure 4. PCI image of the compaction on lattice SN01 (Top) and the simulated radiographs generated by CTH (bottom). The numbers above each image set represent the timing of the images in nanoseconds relative to the triggering event.

To show the robustness of this methodology,

Figure 5 through

Figure 8 compare the recorded PCI images with the simulated radiographs generated by CTH for lattices SN02, SN03, SN57, and SN89, respectively. Again, the PCI images are on top and the CTH simulated radiographs are on the bottom. The numbers above each image set represent the offset of the image in nanoseconds relative to the triggering event. The comparison for lattice SN02, shown in

Figure 5, exhibits excellent agreement in the shape of the compaction wave. In the third and fourth frame, distinct localization (arrows) of material at the compaction front was observed and modeled accurately. Additionally, the CTH simulations adequately captured the ejecta generated from the compaction at this high impact velocity as seen in the last frames (red circle). Although ejecta or failure of material ahead of the compaction wave is an interesting phenomenon, higher impact velocities lead to more of a hydrodynamic response that is less dependent on an accurate

constitutive model. Thus, for the remaining experiments we chose lower impact velocities (\sim 0.6-0.8 km/s) for lattices SN03, SN57, and SN89, shown in Figure 6 through

Figure 8. At these lower impact velocities there is good agreement in the shape of the compaction wave with respect to the simulation and experiment

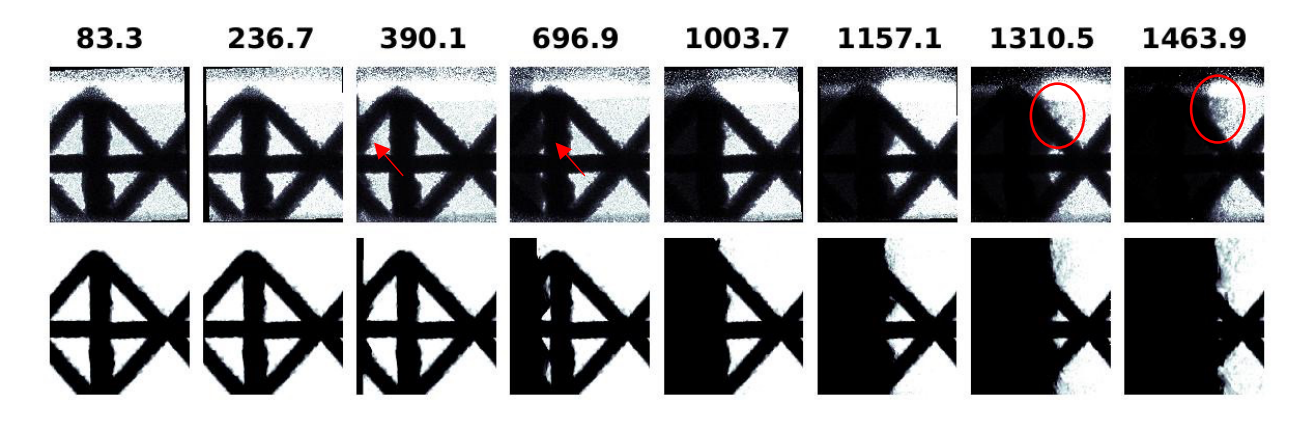


Figure 5. PCI image of the compaction of lattice SN02 (Top) and the simulated radiographs generated by CTH (bottom). The numbers above each image set represent the timing of the images in nanoseconds relative to the triggering event.

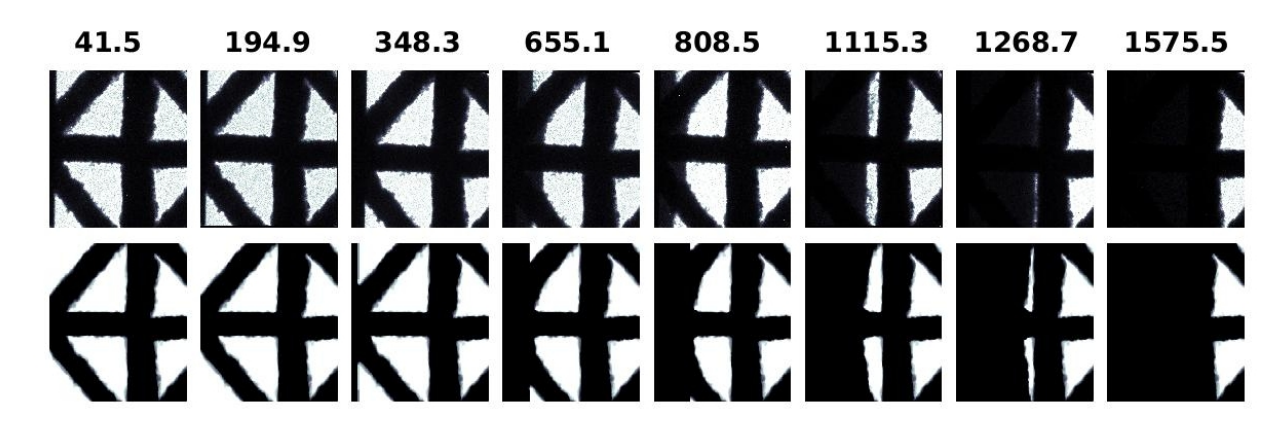


Figure 6. PCI image of the compaction of lattice SN03 (Top) and the simulated radiographs generated by CTH (bottom). The numbers above each image set represent the timing of the images in nanoseconds relative to the triggering event.

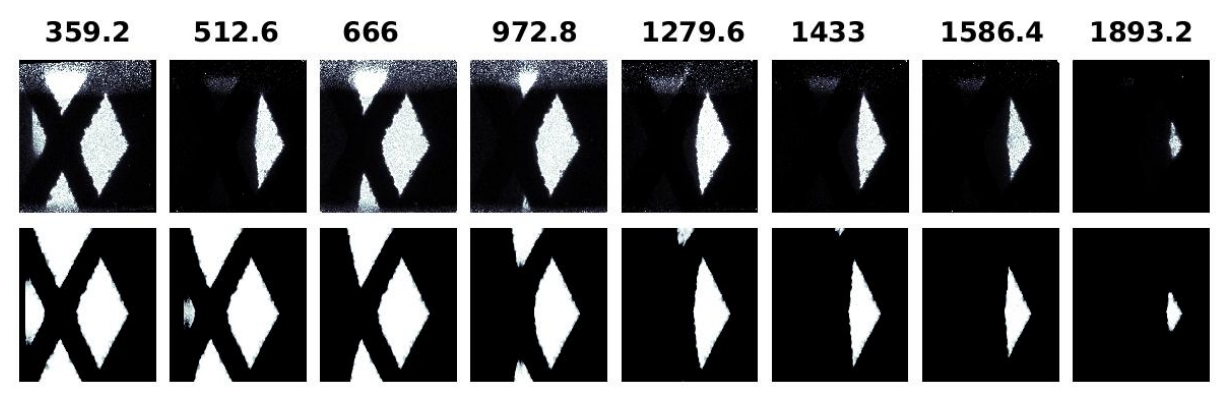


Figure 7. PCI image of the compaction of lattice SN57 (Top) and the simulated radiographs generated by CTH (bottom). The numbers above each image set represent the timing of the images in nanoseconds relative to the triggering event.

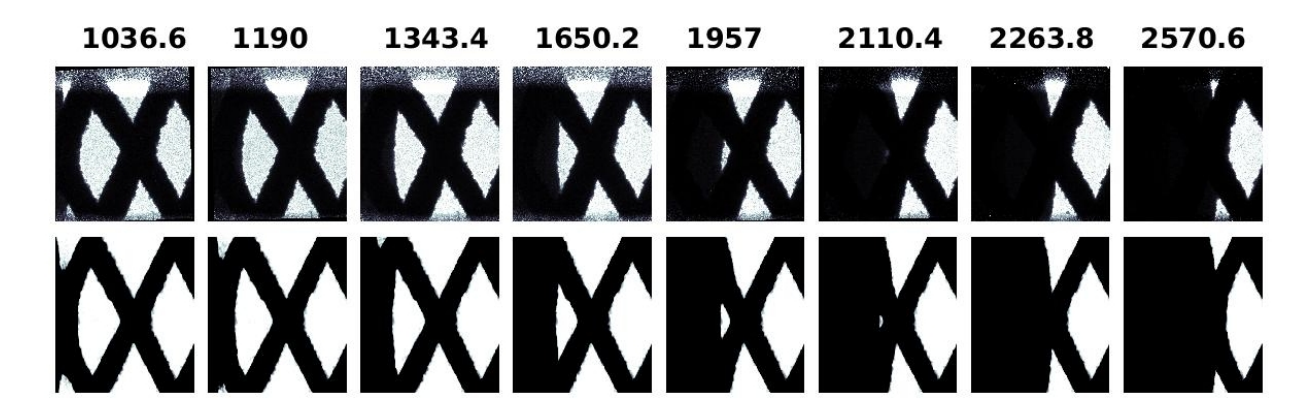


Figure 8. PCI image of the compaction of lattice SN89 (Top) and the simulated radiographs generated by CTH (bottom). The numbers above each image set represent the timing of the images in nanoseconds relative to the triggering event.

Using this methodology, the parameters of the constitutive model can be changed to try and achieve better agreement between the PCI images and simulated radiographs. To illustrate this, the SN01 lattice was simulated with differing strength models, since it was at the lowest impact velocity where constitutive parameters have the largest effect on the compaction response. A comparison of the simulated radiographs from the simulations with differing strength models to the PCI images is shown in

Figure 9. The first set of simulated radiographs (Cal.) are for the calibrated SG model with the initial yield strength increased to match quasi-static data on the AM 316L stainless steel and are identical to those in

Figure 4. The second set of simulated radiographs is for an elastically-perfectly-plastic (EPP) model for the AM 316L stainless steel with an initial yield equal to that measured in the quasistatic experiments. The third set of simulated radiographs is for a SG model where the initial yield point is set to the maximum allowable for strain hardening, 2.5 GPa (High Y). The last set of simulated radiographs is for a purely hydrodynamic simulation (Hydro) were the AM 316L stainless steel is given no strength. One can see that changes in the strength model alter the shape of the compaction wave. When no material strength is considered, one sees that

significant amount of ejecta is generated by the collapse of the lattice. The comparison of simulations with varying constitutive properties to in-situ x-ray phase contrast images demonstrates a more direct validation technique than previously afforded.

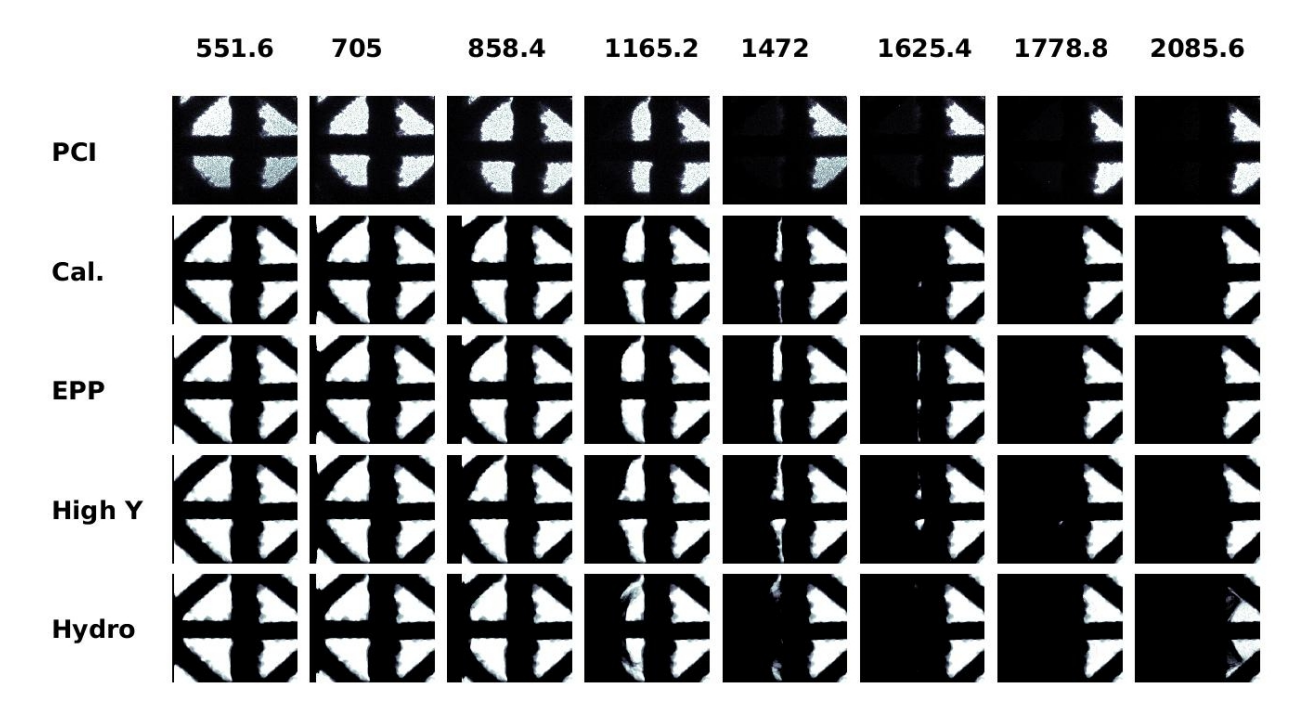


Figure 9. PCI image of the compaction of lattice SN01 (PCI) and the simulated radiographs generated by CTH for various strength models: using the calibrated SG parameters and the initial yield point as determined through quasi-static measurements (Cal.), an elastically-perfectly-plastic model using an initial yield point as defined by quasi-static measurements (EPP), a SG model with the initial yield point set at the maximum for strain hardening (High Y), and a purely hydrodynamic simulations with no strength model (Hydro). The choice of strength model is seen to alter the shape of the compaction wave, with the hydrodynamic case generating a significant amount of ejecta.

4. **CONCLUSIONS**

The unique methodology presented here incorporates as-built lattice geometries into CTH to produce simulated radiographs for direct comparison to in situ x-ray phase contrast images coupled to shock compression experiments. We demonstrate a technique to incorporate the as-built lattice using 2D image slices from CT scans to construct a three-dimensional rendering of the lattice structure in CTH. This allows for divergence from the idealized CAD printing file used during laser powder bed fusion AM deposition (i.e. strut diameter, defects, porosity, etc.) to be accounted for in the meso-scale simulation. This capability to produce simulated radiographs or one-to-one comparison to PCI experiments enables in-depth analysis of how material properties affect the compaction dynamics in 316L stainless steel lattices. The ability to parameterize a constitutive module to such multi-dimension loading provides unprecedented insight into the dynamic behavior of metallic lattices.

REFERENCES

- M. F. Ashby, N. A. Fleck, and A. Evans, *Metal Foams: A Design Guide* (Butterworth-Heinemann, USA, 2000).
- U. Simsek, T. Arslan, B. Kavas, C. E. Gayir, and P. Sendur, International Journal of Advanced Manufacturing Technology.
- J. Niu, H. L. Choo, W. Sun, and S. H. Mok, Journal of Manufacturing Science and Engineering-Transactions of the Asme **140** (2018).
- R. Gumruk and R. A. W. Mines, International Journal of Mechanical Sciences **68**, 125 (2013).
- O. Cervinek, B. Werner, D. Koutny, O. Vaverka, L. Pantelejev, and D. Palousek, Materials **14** (2021).
- J. Choi and T. S. Chae, International Journal of Mechanics and Materials in Design 11, 91 (2015).
- E. Ptochos and G. Labeas, Journal of Sandwich Structures & Materials 14, 597 (2012).
- Q. X. Feng, Q. Tang, S. Soe, Y. Liu, and R. Setchi, in *Sustainable Design and Manufacturing 2016*; *Vol. 52*, edited by R. Setchi, R. J. Howlett, Y. Liu, and P. Theobald (2016), p. 399.
- R. Gumruk and A. Usun, Journal of the Faculty of Engineering and Architecture of Gazi University **35**, 1783 (2020).
- Q. X. Feng, Q. Tang, Z. M. Liu, Y. Liu, and R. Setchi, Proceedings of the Institution of Mechanical Engineers Part B-Journal of Engineering Manufacture **232**, 1719 (2018).
- M. M. Osman, M. Shazly, E. A. El-Danaf, P. Jamshidi, and M. M. Attallah, Composites Part B-Engineering **184** (2020).
- K. Ushijima, D. H. Chen, and W. J. Cantwell, in *Advances in Fracture and Damage Mechanics Xii*; *Vol.* 577-578, edited by A. Milazzo and M. H. Aliabadi (2014), p. 425.
- M. Zhao, F. Liu, G. Fu, D. Z. Zhang, T. Zhang, and H. L. Zhou, Materials 11 (2018).
- R. Xue, X. G. Cui, P. Zhang, K. Liu, Y. Li, W. W. Wu, and H. T. Liao, Extreme Mechanics Letters **40** (2020).
- P. Wang, Y. J. Bian, F. Yang, H. L. Fan, and B. L. Zheng, Acta Mechanica **231**, 3129 (2020).
- M. T. Hsieh, B. Endo, Y. F. Zhang, J. Bauer, and L. Valdevit, Journal of the Mechanics and Physics of Solids **125**, 401 (2019).
- D. T. Queheillalt and H. N. G. Wadley, Acta Materialia **53**, 303 (2005).
- J. C. Wallach and L. J. Gibson, International Journal of Solids and Structures **38**, 7181 (2001).
- B. Hanks, J. Berthel, M. Frecker, and T. W. Simpson, Additive Manufacturing **35** (2020).
- ²⁰ T. L. Zhong, K. T. He, H. X. Li, and L. C. Yang, Materials & Design **181** (2019).
- I. Maskery, A. O. Aremu, M. Simonelli, C. Tuck, R. D. Wildman, I. A. Ashcroft, and R. J. M. Hague, Experimental Mechanics **55**, 1261 (2015).
- Y. H. Zhang, X. M. Qu, and D. N. Fang, International Journal of Solids and Structures **45**, 3751 (2008).
- A. D. Dressler, E. W. Jost, J. C. Miers, D. G. Moore, C. C. Seepersad, and B. L. Boyce, Additive Manufacturing **28**, 692 (2019).
- G. T. Gray, V. Livescu, P. A. Rigg, C. P. Trujillo, C. M. Cady, S. R. Chen, J. S. Carpenter, T. J. Lienert, and S. J. Fensin, Acta Materialia **138**, 140 (2017).

- Y. H. Chen, S. J. Clark, D. M. Collins, S. Marussi, S. A. Hunt, D. M. Fenech, T. Connolley, R. C. Atwood, O. V. Magdysyuk, G. J. Baxter, M. A. Jones, C. L. A. Leung, and P. D. Lee, Acta Materialia 209 (2021).
- P. Spoerk-Erdely, P. Staron, J. Liu, N. Kashaev, A. Stark, K. Hauschildt, E. Maawad, S. Mayer, and H. Clemens, Advanced Engineering Materials.
- L. Sinclair, C. L. A. Leung, S. Marussi, S. J. Clark, Y. H. Chen, M. P. Olbinado, A. Rack, J. Gardy, G. J. Baxter, and P. D. Lee, Additive Manufacturing **36** (2020).
- S. Karagadde, C. L. A. Leung, and P. D. Lee, Materials 14 (2021).
- S. J. Wolff, S. Webster, N. D. Parab, B. Aronson, B. Gould, A. Greco, and T. Sun, Jom 73, 189 (2021).
- M. R. Khosravani and T. Reinicke, Journal of Nondestructive Evaluation **39** (2020).
- E. Hernández-Nava, S. Tammas-Williams, C. Smith, F. Leonard, P. Withers, I. Todd, and R. Goodall, Metals **7**, 300 (2017).
- N. C. Ferreri, R. Pokharel, V. Livescu, D. W. Brown, M. Knezevic, J. S. Park, M. A. Torrez, and G. T. Gray, Acta Materialia **195**, 59 (2020).
- X. Y. Chen, Q. X. Ji, J. Z. Wei, H. F. Tan, J. X. Yu, P. F. Zhang, V. Laude, and M. Kadic, International Journal of Mechanical Sciences **169** (2020).
- ³⁴ X. F. Cao, X. B. Ren, T. Zhao, Y. Li, D. B. Xiao, and D. N. Fang, International Journal of Mechanics and Materials in Design **17**, 271 (2021).
- D. M. Dattelbaum, A. Ionita, B. M. Patterson, B. A. Branch, and L. Kuettner, **10**, 075016 (2020).
- B. Branch, A. Ionita, B. E. Clements, D. S. Montgomery, B. J. Jensen, B. Patterson, A. Schmalzer, A. Mueller, and D. M. Dattelbaum, Journal of Applied Physics **121** (2017).
- B. Branch, A. Ionita, B. M. Patterson, A. Schmalzer, B. Clements, A. Mueller, and D. M. Dattelbaum, Polymer **160**, 325 (2019).
- J. Lind, B. J. Jensen, M. Barham, and M. Kumar, Journal of Materials Research **34**, 2 (2019).
- ³⁹ CTH v12.0, Sandia National Laboratories (2017).
- D. H. Dolan, T. Ao, and S. C. Grant, "The Sandia Matlab AnalysiS Hierarchy (SMASH) Toolbox," (2016).
- P. E. Specht, "Shock Compression Resposne of Aluminum-Based Intermetallic-Forming Reactive Systems," (2013).
- B. A. Branch, G. Frank, A. Abbott, D. Lacina, D. M. Dattelbaum, C. Neel, and J. Spowart, Journal of Applied Physics **128**, 245903 (2020).
- B. J. Jensen, S. N. Luo, D. E. Hooks, K. Fezzaa, K. J. Ramos, J. D. Yeager, K. Kwiatkowski, T. Shimada, and D. M. Dattelbaum, Aip Advances **2**, 6 (2012).
- S. N. Luo, B. J. Jensen, D. E. Hooks, K. Fezzaa, K. J. Ramos, J. D. Yeager, K. Kwiatkowski, and T. Shimada, Review of Scientific Instruments **83**, 10 (2012).
- K. S. Holian, "T-4 Handbook of Material Properites Data Bases," (1984).
- D. J. Steinberg, S. G. Cochran, and M. W. Guinan, Journal of Applied Physics **51**, 1498 (1980).
- D. Steinberg, *Equation of state and strength properties of selected materials* (Lawrence Livermore National Laboratory, Livermore, CA, 1996).
- ⁴⁸ Z. J. Casias and J. Carroll.
- G. I. Kerley, International Journal of Impact Engineering **5**, 441 (1987).

DISTRIBUTION

Email—Internal

Name	Org.	Sandia Email Address
Bradley Jared	01832	bhjared@sandia.gov
Scott Jensen	01832	scjense@sandia.gov
Brad Boyce	01881	blboyce@sandia.gov
Michael Heiden	01832	mheiden@lanl.gov
Jonathan Pegues	01832	jwpegue@sandia.gov
Chris Seagle	01646	ctseagl@sandia.gov
Technical Library	01977	sanddocs@sandia.gov



Sandia National Laboratories is a multimission laboratory managed and operated by National Technology & Engineering Solutions of Sandia LLC, a wholly owned subsidiary of Honeywell International Inc. for the U.S. Department of Energy's National Nuclear Security Administration under contract DE-NA0003525.